Surface roughness control in deep engraving of fused silica using femtosecond laser ablation

Evaldas Kažukauskas *, Simas Butkus, Vytautas Jukna, Domas Paipulas

Laser Research Center, Faculty of Physics, Vilnius University, Saulėtekio Ave. 10, Vilnius, LT-10223, Lithuania

ARTICLE INFO

ABSTRACT

The capability to control the surface morphology during ultrafast laser micromachining at different engraved depths for transparent dielectric materials is of great importance in many applications, such as micromechanics, free-form optics, medical implants. The precise surface roughness management during deep engraving in most cases can be achieved by fine tuning of laser and scanning parameters utilizing material-dependent optimization strategies. In this study, we have compared and investigated the influence of different laser scanning algorithms for deep engraving of fused silica in order to establish the methods capable to provide a flexible control on machined surface roughness. We show that control of surface roughness in a broad range $\Delta S_a \sim 550$ nm is possible with a resolution of $\delta S_a = 20$ nm, with the possibility to reduce surface roughness down to ~ 100 nm without any post-processing. While the achieved values demonstrated in this work are wavelength-, algorithm- and material-dependant, we provide the general processing strategy that could nullify discrete laser patterning artefacts, while the magnitude of laser-induced nanostructures dictates the lower limit of resulting surface roughness in ultrafast laser processing.

1. Introduction

Surface machining for shape retrieval or changing its optical, chemical, mechanical, and other physical properties has been in demand for many applications. The biggest part of today's industry is based on conventional mechanical surface treatment methods such as CNC (computer numerical control) milling, turning, and abrasive polishing [1], although other more sophisticated methods like chemical treatment, electro-polishing, or lithography have also found their place for smaller scale unique applications [2–4]. In the past few decades, the development of advanced and dependable lasers has made laser radiation an increasingly popular surface treatment technique for a wide range of materials. This method offers numerous advantages over traditional approaches, including exceptional precision, versatility, and more [5]. A conventional way to form any shape using laser radiation is by selectively ablating the material layer by layer until the desired shape is achieved. Such a way of removing material is known as laser engraving.

During laser engraving, the topography of the surface and its roughness changes due to interaction with the laser radiation. It is well known that surface roughness is an important parameter that dramatically influences various material properties. It was shown that for many types of metals, the roughness determines the rate of corrosion [6] and wettability properties [7]. In addition, the wear rate of aircraft engine parts is also directly related to the surface roughness [8]. Surface roughness has an impact on fluid dynamics [9,10] and optical properties like absorption, reflection, and transparency [11–13]. Surface topography can act as an antibacterial coating under distinct surface morphology and roughness configurations [14]. For these reasons, the ability to control the surface roughness during the process of laser engraving is highly desired.

A standard way to achieve the desired surface roughness after the laser ablation is by conducting a parametric laser surface processing study [15–17]. When working with metals, the optimization results show that the smoothest surface is achieved by operating at fluencies that produce the highest ablation efficiency while maintaining a high pulse overlap of over 60% [17]. However, when ablating silicon, it was shown that lower overlap of 20% results in minimum roughness [18]. Yet, some studied utilizing different laser configuration reports a higher overlap (60%) requirements for minimum roughness [19]. The contradicting results show that optimal processing parameters vary for different materials and are not universal, also there is a lack of systematic research on the application of ultrafast pulses for deep-engraving of dielectrics, leaving the possibilities for roughness control unanswered.

The approach of conducting parametric studies for surface roughness optimization is not very convenient, as it is developed for a single

---

* Corresponding author.
E-mail address: evaldas.kazukauskas@ff.vu.lt (E. Kažukauskas).

material under a strict laser configuration. More sophisticated optimization techniques can include the use of the "design of experiment" models for reducing parameter space (e.g. Taguchi method [20,21]) or machine learning models based on neural networks [22,23]. While the former method holds promising potential for the future, its current utility is limited by the absence of databases necessary for model training. Another, completely different, but promising way to control the surface roughness is by implementing different scanning algorithms, rather than changing laser parameters. Using this approach, the pulse energy is fixed while laser scanning parameters are varied to achieve diverse processing results [24,25].

In our recent work [26], we conducted an in-depth investigation on how various scanning algorithms impact the resulting surface roughness when the glass surface is subjected to a single scan, resulting in removal of only a few micrometers of material. Dependencies of resulting roughness on the overlap of craters, patterning strategies, scanner-laser synchronization were established and discussed. In deep-engraving, to achieve the desired depths, the surface must undergo multiple scanning iterations. Only a few studies can be found in the literature that explore the surface roughness changes regarding scanning algorithms in repetitive processing in metallic [27,28] or dielectric materials [29,30].

In this study, we have investigated different scanning algorithms and their effectiveness in controlling the surface roughness when surface is scanned multiple times. Our findings indicate that certain scanning algorithms with added layer positioning uncertainties and the rotations of the scanning patterns allow for achieving the roughness saturation within the first several tens of scans. Moreover, the saturation level can be varied in a broad range by controlling the overlap and the depth of the craters. Finally, we demonstrate that the combined use of these algorithms enables the comprehensive control of surface roughness during deep engraving.

2. Materials and methods

In this study, a femtosecond Yb:KGW laser ("Carbide", manufactured by Light Conversion Ltd.) with an average power of 40 W and pulse duration of 211 fs at full width half maximum (FWHM) was used as a light source. The laser was operating at a 100 kHz repetition rate, generating 1030 nm center wavelength (1H) laser radiation. In some experiments, the UV laser radiation (343 nm) generated with an external third harmonic (3H) generation module was used. The pulse energy was varied using an external attenuator that consisted of $\lambda/2$ waveplate and a brewster-type polarizer (see Fig. 1). The laser beam was guided to a galvanometer scanner ("IntelliSCAN10$_{se}$", SCANLAB Ltd.) via high-reflectivity dielectric mirrors. The laser beam was focused on the top of the sample using a 100 mm focal length f-theta lens. For the UV wavelength, the beam path was identical just the attenuation, dielectric mirrors, and f-theta lens were chosen to suit this wavelength. The beam diameter at the lens focus was measured to be 21 μm (1H), and 12.6 μm (3H). Measurements were done by the well known Liu method [31].

The scanner was mounted on the nanopositioning stage ("ABL1500", AEROTECH) that allowed movement in the z direction, i.e. perpendicular to the sample surface. This allowed us to adjust the distance from the lens to the surface of the sample during the deep-engraving procedure to ensure that processing is maintained in the focal plane of the lens. For convenience, the sample was additionally placed on the nanopositioning stages ("ABL1500WB", AEROTECH) enabling the precise positioning in x and y directions.

The experiments were carried out on 1 mm-thick fused silica glass samples. Laser engraving and surface microstructuring was done with the first harmonic (1030 nm) and third harmonic (343 nm) wavelengths. The third harmonic was used only when smaller diameter

craters were needed to benchmark the lowest achievable surface roughness. Using the previously mentioned Liu method, the ablation threshold of fused silica samples for the fundamental wavelength was determined to be $F_{th} = 3.1$ J/cm^2 (for a single pulse). The initial sample surface roughness was measured to be $S_a = 5$ nm. The measured value falls within the range of the device's measurement noise, indicating that the real initial roughness value is $S_a \leq 5$ nm.

The experiments consisted of scanning a surface area of 1×1 mm^2 multiple times with the scanner by a chosen scanning algorithm. After each experiment, the sample was repositioned at the center of the lens field with the assistance of the x and y translation stage. In our setup, the laser pulse triggering and scanner position were electronically synchronized (using the functionality of scanner control board "RTC5" (SCANLAB Ltd.)), meaning that the positioning uncertainty of the first pulse position in a line is removed. Without the synchronization, the positioning uncertainty arises which eventually leads to the variations in surface roughness according to surface orientation as was observed in our previous work [26].

It was established that the overlap of the craters in x and y directions (see Fig. 2(A)) during the engraving is an important factor that greatly impacts final roughness [26]. The overlap in x direction (along laser scanning path) was realized by tailoring the scanning speed and the gating frequency. While overlap in the y direction (perpendicular to the scanning) was acquired by setting the distance between adjacent lines. We have chosen the overlap in the longitudinal and transverse directions to be identical. The overlap of craters was defined as [32]

$$\Omega = (1 - \frac{dx}{D}) \times 100\%, \tag{1}$$

here Ω - the overlap of craters in percents, dx - the distance between adjacent craters, D - the diameter of a single crater.

In our study, several different scanning strategies were investigated for multilayered processing. The first one included the rotation of every next layer at a fixed angle relative to the previous one. The axis of rotation was set to be at the center of the machined area. By utilizing different angles of rotation, various patterns could be generated that produce different values of surface roughness (see Fig. 2(B)). The second scanning strategy was the introduction of the randomized displacement of the rotation axis within each layer (see Fig. 2(C)). The use of this strategy assisted in preventing the formation of patterning artefacts that are formed otherwise, and led to the reduction of final surface roughness. Finally, the last strategy involved adjusting the laser (pulse energy) and scanning (overlap of the craters, see Fig. 2(A)) parameters for the control of the resulting surface morphology. For the realization of the scanning algorithms and laser processing automation, the commercial laser processing software DMC (Direct Machining Control, Ltd.) was used.

The laser-processed areas were subjected to the surface roughness measurements after the machining. The laser scanning microscope ("LEXT OLS5100", Olympus) equipped with a 100x (0.8 NA) objective was used for the acquisition of the surface topographies. The samples were centered on proceesed region and the surface region of 256 μm × 256 μm (comprising 2048 × 2048 measuring points) was captured. A surface roughness parameter - arithmetical mean height (S_a) - was computed for each surface as per ISO 25178 standard, with the mathematical expression provided in the equation:

$$S_a = \frac{1}{A} \iint_A |z(x,y)| dx dy. \tag{2}$$

Here A is the value of the evaluation area and $z(x,y)$ is the absolute height deviation from an average value at x and y coordinates. The scope of this study is to showcase the ability to control the surface roughness using different scanning algorithms, therefore assessing only the average roughness values proved to sufficient. Fallowing ISO standard procedure, we applied S (surface small-scale) and F (form removal) filters, while L (surface large-scale) filter was excluded. Therefore, the surface roughness parameter S_a constitutes the average
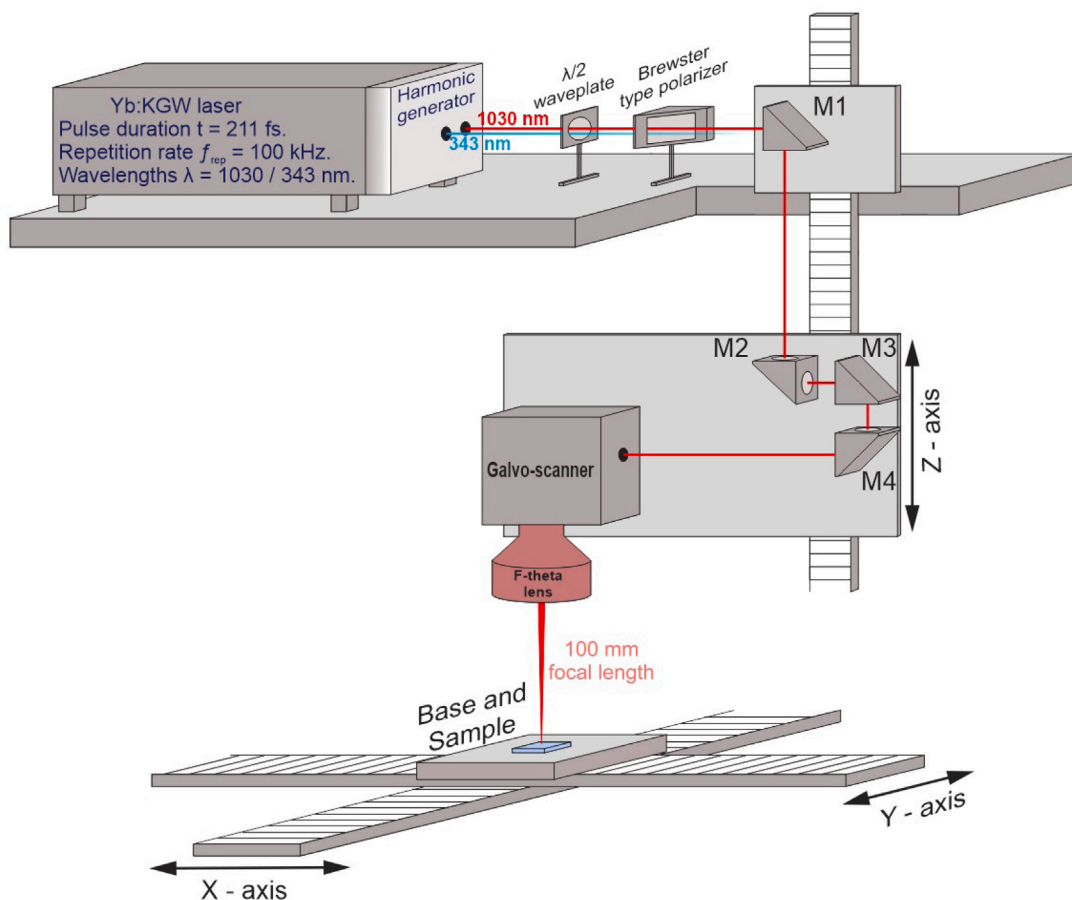
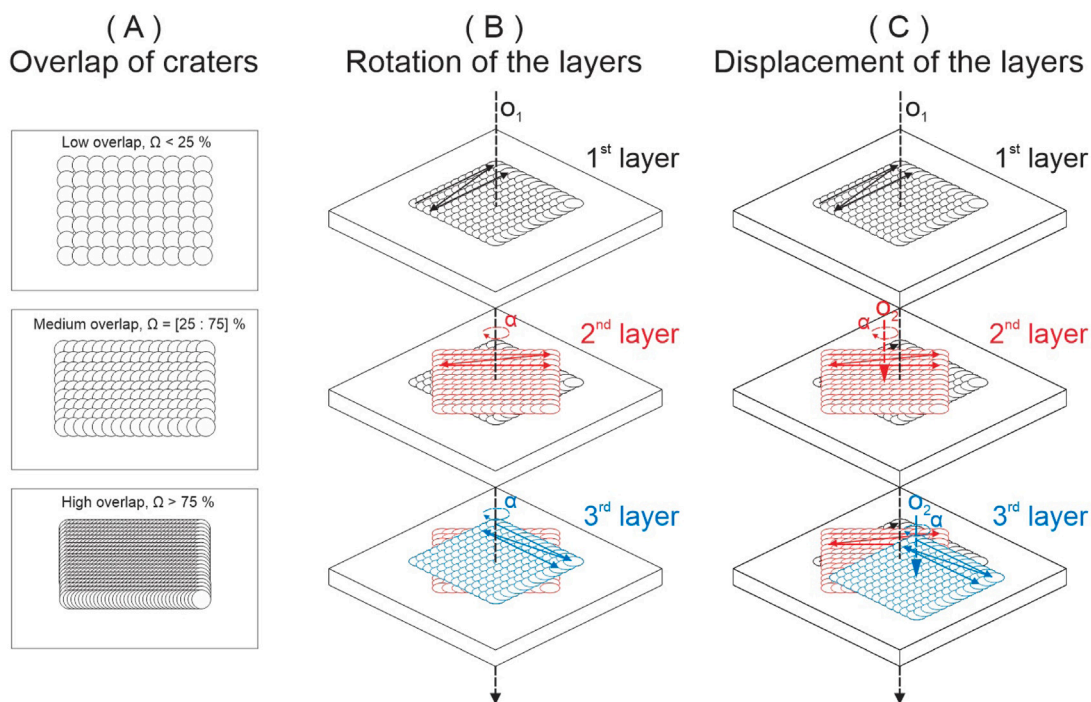**Fig. 1.** Experimental setup used for deep engraving of fused silica.

Fig. 2. The visual representation of different scanning algorithms used throughout the study. The investigated algorithms were: (A) the changing of the overlap of the craters, (B) the rotation of the subsequent layers around the common axis o by angle α, and (C) introducing the displacement of the layers with each rotation. Here, the letters o_n represent the centers of each layer. Different colors stand for different layers. (For interpretation of the references to color in this figure legend, the reader is referred to the web version of this article.)
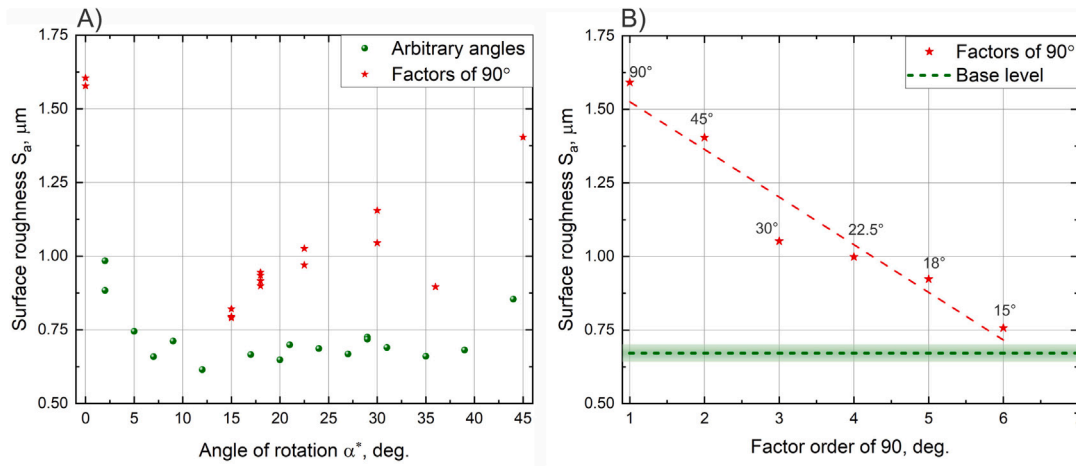
Fig. 3. (A) The surface roughness dependence on the angle (α) of layer rotation, when surface is scanned 30 times. Two distinctive angle categories are depicted: arbitrary angles and factors of 90°. Due to truncation operation, certain angles of rotation are represented by multiple roughness values (see text for details). (B) The dependence of the surface roughness on the factors of 90°. The fit is presented as a red dashed line, whereas the base level formed of arbitrary angles is presented as a green dashed line with a standard deviation (1σ) shown as a green area. Processing parameters: fluence F = 52 J/cm^2, overlap of the craters Ω = 20%, wavelength λ = 1030 nm. (For interpretation of the references to color in this figure legend, the reader is referred to the web version of this article.)
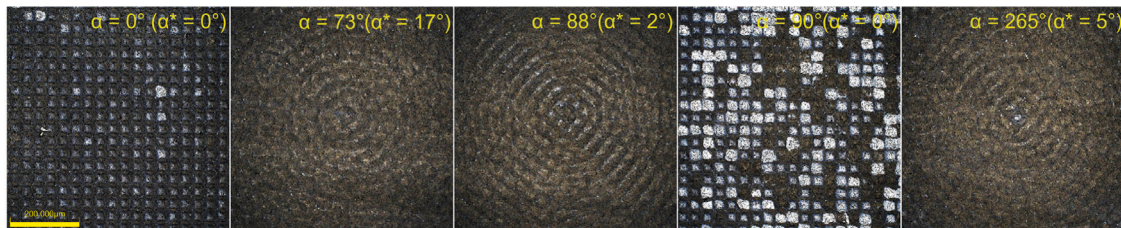

Fig. 4. Extended color images of surface structures induced by scanning the surface 30 times with different angles of rotation (α). Fluence F = 52 J/cm^2, overlap of the craters Ω = 20 %, wavelength λ = 1030 nm. (Note: images are acquired with optical profilometer by combining the stack of images made at different focus position to achieve a single all-in-focus image, for this reason reflected light intensity is not homogeneous and brighter regions appear at deeper pits).

roughness of a scale-limited SF surface. For the removal of the small-scale lateral components that denote measurement noise, the nesting index of 0.5 μm was applied. To remove the tilt induced by inaccurate positioning of the sample, a best-fit least squared F operation was executed. The measurement noise was determined using the subtraction technique [33]: from a set of 10 measurements, the noise value, expressed as the root mean square of roughness was estimated to be 6.5 nm.

Microscope images presented in the study were acquired using the same laser scanning microscope "LEXT OLS5100", while SEM inspection was carried out with Thermo Scientific "Prisma E" microscope. Finally, the energy-dispersive X-ray spectroscopy of the samples was carried out using the "INCA Energy 350 X-Max 20 EDX" spectrometer (Oxford Instruments).

3. Results and discussion

In previous work [26], we have investigated the surface roughness dependencies on different scanning algorithms when the surface is scanned only one time. It was shown that minimum surface roughness is achieved when the overlap of ablated craters (Ω) is in the range of 10%–25%. Under such conditions only steep crater edges are repeatedly ablated while relatively flat bottoms remain underexposed, resulting in a smooth surface. Therefore in initial experiments of this study a fixed overlap of 20% was used.

In first stage, an investigation of surface roughness evolution when every consecutive layer is rotated by a particular angle was carried out (see Fig. 2(B)). The angle at which the nth layer was rotated can be expressed with the following equation:

$$\alpha_n = (n-1) \times \alpha, \tag{3}$$

here, α_n - the angle at which the nth layer is rotated, n - the layer number, α - the angle of rotation.

Each processed area was scanned 30 times with a fixed angle of rotation (α) and the resulting surface roughness was measured. The resultant dependence is presented in Fig. 3, while microscope images of selected surfaces are shown in Fig. 4. The full range of angles from 0° to 360° were investigated. After examining the results, it was observed that two categories of angles can be identified: the category 1 comprises arbitrary angles (depicted as green circles in Fig. 3) and include primary numbers such as 3°, 29°, 73°; while the category 2 include particular angles that are factors of 360° (shown as red stars). With category 1 angles, the initial crater pattern seldom matches with successive pattern, while for angles of category 2 partial alignment with the preceding layer takes place, producing distinctive laser patterning artefacts on the surface. Given the directional symmetry of the layer rotation, where both clockwise and anti-clockwise rotations have an identical effect on the quadratic pattern, the complete angular range can be truncated to [0°; 45°] interval using triangular function:

$$\alpha^* = \frac{1}{4}\cos^{-1}[\cos(4\alpha)], \tag{4}$$

here α^* is a truncated angle. Using such conversion, the category 2 angles become factors of 90°.

The surface roughness dependence on the compressed domain of angles is shown in Fig. 3(A). Bigger arbitrary angles produce almost constant surface roughness (in this example $S_a \sim 0.65$ μm), while category 2 angles exhibit rise in roughness. This is expected result, as the laser beam in the former case is repositioned in the same locations as in the previous layers, resulting in the formation of deeper localized valleys. This generates high-contrast periodic structures (see Fig. 4, α = 0°, 90°) that yield high surface roughness ($S_a > 0.8$ μm). Results show
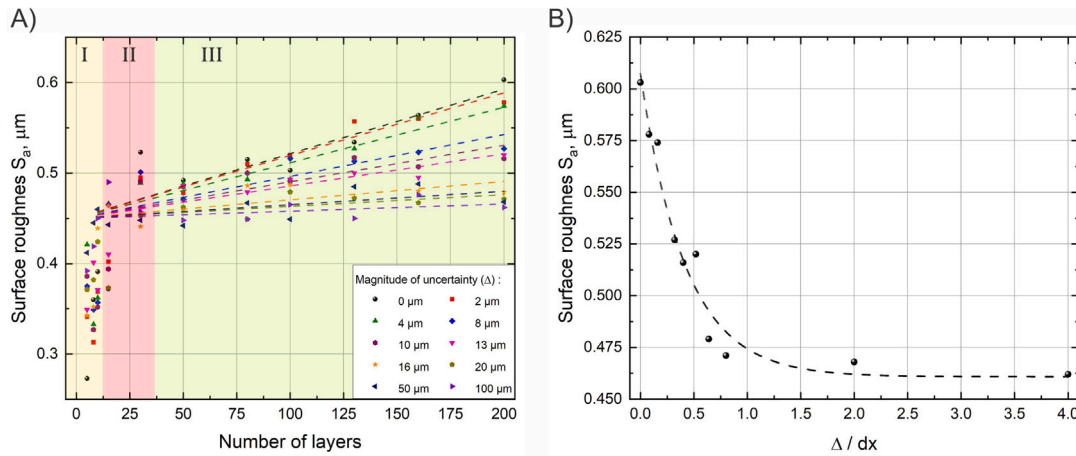
Fig. 5. (A) Surface roughness (S_a) dependence on the number of layers, when layer positioning uncertainty is introduced. Symbols represent raw data, dashed lines — linear fits of the data within the region III (see text for details). (B) A surface roughness dependence on the magnitude of layer positioning uncertainty divided by a pulse-to-pulse pitch after 200 layer processing. Symbols represent raw data, whereas the dashed lines show a decaying exponential fit. Processing parameters: overlap of the craters $\Omega = 22\%$, fluence $F = 20.8$ J/cm^2, wavelength $\lambda = 1030$ nm, diameter of a single crater $D = 32$ μm, pulse-to-pulse pitch - 25 μm.
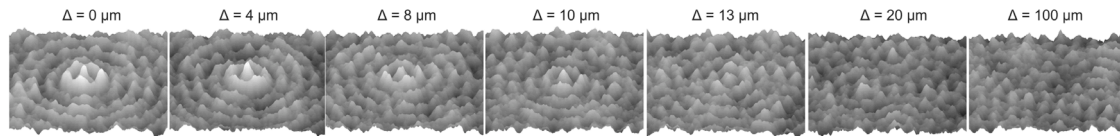

Fig. 6. 3D views of engraved regions after 200 layers of processing with different layer positioning uncertainties. Dimensions of a single window 250×250 μm. Processing parameters: overlap of the craters $\Omega = 22\%$, fluence $F = 20.8$ J/cm^2, wavelength $\lambda = 1030$ nm, diameter of a single crater $D = 32$ μm, pulse-to-pulse pitch - 25 μm.

that the increase in the factor order linearly reduces surface roughness (Fig. 3(B)). Rotation of layer by 90°, yield the same pattern at each scan (for the quadratic pattern with rotational axis fixed on the center); however, if a 30° angle is used, the scanning pattern coincides only with every 3rd layer, and so on. When category 2 angle exceeds the 6th factor, surface roughness approaches the values achievable with arbitrary angles. Hence, when aiming to minimize surface roughness, it is crucial to stay away from category 2 angles.

Despite the minimal roughness, the distinctive periodic artefacts having circular symmetry with dip in the center is present in all category 1 angle cases as seen in the microscope pictures (Fig. 4). Again, this effect is expected, as rotational axis remains constant throughout processing, and attributes to continuous growth of the roughness. Such patterning structures in multiscan processing can be avoided by implementing the "shifting axis of rotation" technique. This method involves moving the axis of rotation to a different position during each scanning iteration. In practice, this can be realized by introducing the uncertainty in layer positioning defined by the equations:

$$X_{poz} = X_{org} + (\Re - 0.5) \times \Delta, \tag{5}$$

$$Y_{poz} = Y_{org} + (\Re - 0.5) \times \Delta. \tag{6}$$

Here X_{org}, Y_{org} are the initial coordinates of the central point of the micro-machined area, which also serves as the axis of rotation, whereas X_{poz}, Y_{poz} are the coordinates of the axis of rotation after the introduction of layer positioning uncertainty. $\Re$ is a function that generates a random number from a continuous uniform distribution within the boundaries of [0 1], while Δ defines the maximum magnitude of the uncertainty. In order to examine the impact of layer positioning uncertainty on the surface roughness, the position of the center point of each layer was recalculated according to Eqs. (5), (6), while, the layer rotation was maintained at a category 1 angle ($\alpha = 73°$). The results are depicted in Fig. 5. It can be seen that introducing the uncertainty of the layer positioning has a great impact on the evolution of surface roughness.

The surface roughness evolution during multilayer processing mainly consists of 3 stages (depicted as I, II, and III regions in Fig. 5(A)): initiation (I), transition (II), and saturation (III). In the first stage, which typically happens within the first 10 layers, the roughness increases very rapidly with each successive layer. This growth is expected, as certain amount of layers is required for the establishment of the shape of the ablated surface with selected laser patterning. When the shape is achieved each subsequent layer is used to further engrave the surface, while maintaining the shape. Subsequently, during multipulse irradiation, the laser-induced nanoripples start to form. The formation of self-organized nanostructures in multipulse laser treatment of metals and dielectrics is a widely known and intensely studied phenomenon [34–36]. Stage II typically spans across 15 to 30 layers and represents the surface morphology transition from semi-clean to fully covered by nanoripples. It was observed that nanoripple islands close to ripple-free regions have irregular height changes, thus increasing roughness. As a result, when the surface is only partly covered by nanoripples, the surface roughness value peaks (this can be seen by the outliers in region II). However, when the formation of nanoripples across the entire surface is completed, the elevations become more uniform, resulting in a slight reduction in surface roughness. After the transition stage, the subsequent phase, denoted as the final saturation stage (III), commences. When the entire surface is covered by nanoripples, the only variables influencing the final roughness are the crater's shape and its depth. It can be seen that when the rotation axis is fixed, the linear growth of the surface roughness is evident, which is attributed to the growth of the patterning artefacts and their magnitude. However, when the positioning uncertainty is introduced, these artefacts can be prevented (see Fig. 6). By shifting the rotation axis to a slightly different location for each layer and maintaining layer rotation, the likelihood of positioning the laser beam to the same location as in the previous layers significantly decreases, rendering the occurrence of such events negligible. Consequently, the introduction of layer position uncertainty prevents the formation of patterning artefacts, resulting in a randomly patterned structure at the bottom of
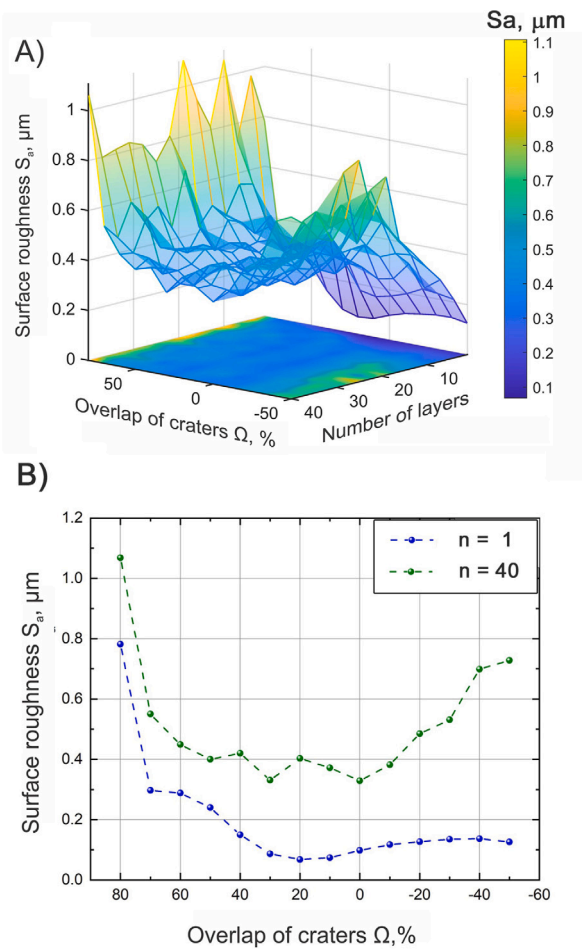
Fig. 7. (A) Surface roughness evolution when different overlaps of the craters are used. (B) Surface roughness dependence on the overlap value in single and multi-scan (40) cases. Processing parameters: Fluence F = 26.1 J/cm^2, angle of rotation $\alpha = 73°$, wavelength $\lambda = 1030$ nm. The uncertainty of layer positioning of a maximum magnitude $\Delta \geq dx$ was maintained. (For interpretation of the references to color in this figure legend, the reader is referred to the web version of this article.)

Fig. 8. (A) Cross-sections of the craters produced using different pulse energies and wavelengths. (B) Surface roughness evolution after subsequent laser scanning with different crater dimensions. (C) Surface roughness dependence on the depth of a single crater after 100 scans when the stabilization of surface roughness is reached. Dots represent experiment data, dashed line — fit of the data. The scanning speed was adjusted to maintain the optimal overlap ($\Omega = 20\%$) in all the cases. In addition, each layer was rotated by 73°. The uncertainty of layer positioning of a maximum magnitude $\Delta \geq dx$ was maintained. (For interpretation of the references to color in this figure legend, the reader is referred to the web version of this article.)

the cavity. Therefore, the roughness value saturates at the beginning of the III stage and remains constant with the increasing number of layers. This results in the reduction of the final roughness compared to the fixed axis case.

The maximum reduction of the surface roughness (from 600 µm down to 460 µm (S_a)) is achieved after 200 layers when the uncertainty parameter $\Delta \geq 25$ µm is used. Since the absolute value of the Δ parameter depends on the chosen patterning algorithm, a more appropriate way is to link it to the pulse-to-pulse pitch (distance between two craters). Since the pitch was fixed to $dx = 25$ µm, the surface roughness after 200 layers dependence on the pitch-normalized uncertainty magnitude can be derived (Fig. 5(B)). We see that the condition for the saturation and the minimization of the roughness can be expressed as $\Delta \geq dx$.

Therefore, introduction of the uncertainty of the layer positioning results in the saturation of the surface roughness, meaning that the number of scans conducted on the surface, whether it be 50, 100, or 200 times, becomes inconsequential as the resulting roughness remains constant. This capability allows for the prediction of the resulting roughness following the machining process for deep engraving applications. Nevertheless, in order to attain complete control over the roughness, it is necessary to possess the ability to change the level at which the roughness saturates.
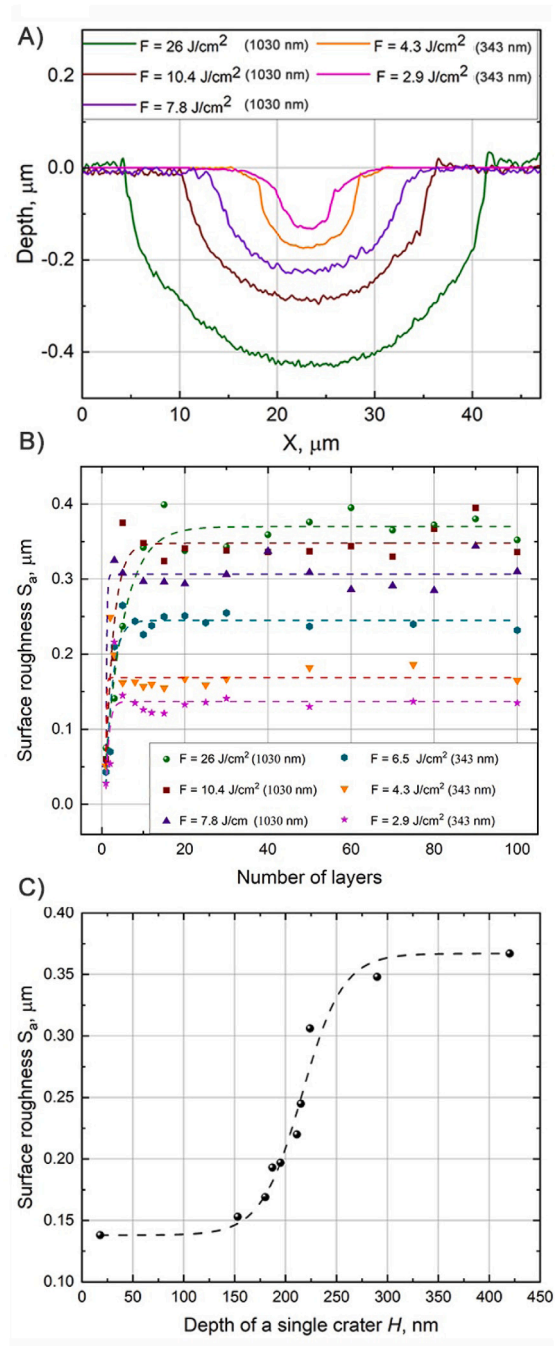
We identified two distinct methods that enable the control at which value roughness can be stabilized. The first one includes tailoring the overlap of the craters. By realizing different overlaps of the craters, surface morphology that yields different roughness values develops [26]. The results on roughness evolution versus crater overlap after multilayer scanning are shown in Fig. 7(A), while Fig. 7(B) depicts results
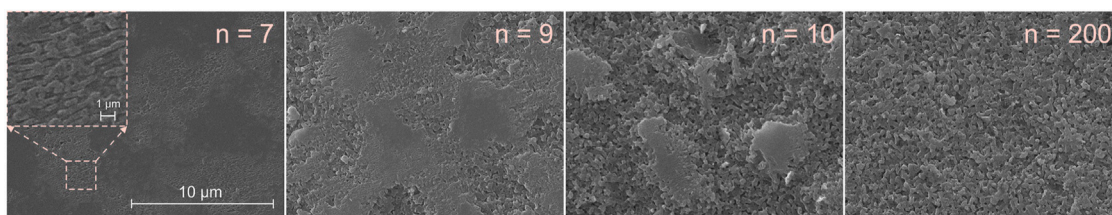
Fig. 9. SEM images of the ablated regions produced after different numbers of scans. Processing parameters: fluence F = 2 J/cm^2, overlap of the craters $\Omega = 20\%$, angle of rotation $\alpha = 73°$, wavelength $\lambda = 343$ nm. The uncertainty of layer positioning of a maximum magnitude $\Delta \geq dx$ was maintained.
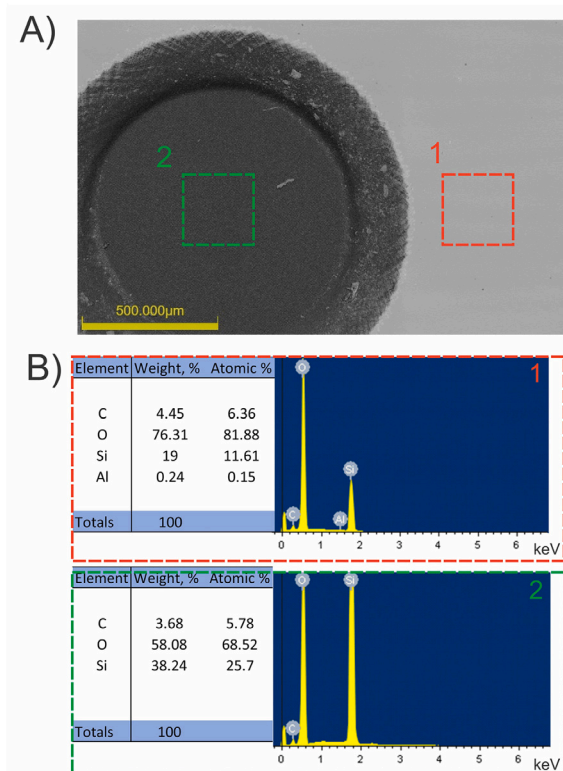

Fig. 10. (A) Microscope image of the sample with partly treated area. The ablated area was achieved using processing parameters: fluence F = 2 J/cm^2, overlap $\Omega = 20\%$, angle of rotation $\alpha = 73°$, wavelength $\lambda = 343$ nm. The uncertainty of layer positioning of a maximum magnitude $\Delta \geq dx$ was maintained. The surface was scanned $n = 200$ times. The (1) and (2) regions indicate the locations where EDS analysis was performed. The corresponding results are shown in (B).

for the initial and final layers. It is clear, that the optimal overlap of the craters ($\Omega = 10-25\%$) for the lowest roughness is maintained even when the surface is scanned multiple times (up to 40 times). Other values of overlaps increase surface roughness.

When dense crater overlap ($\Omega \geq 60\%$) is used, the accumulated fluence may increase to a point where stress-induced cracking becomes present. Such a situation is unique for the glass-type substrates, specifically fused silica, and could differ for other materials. On the other hand, the rise in surface roughness observed at lower values ($\Omega \leq -10\%$) results from sporadic ablation. From Fig. 7(A), we can see that with the introduction of positioning uncertainty and layer rotation at category 1 angle, roughness stabilization can be achieved over multiple scans. This shows that roughness control and stabilization can be achieved using a single technique. However, in special cases, roughness sensitivity to the overlap of the craters is quite severe (i.e. in the range from $\Omega = 60 - 80\%$), implying that the fine-tuning of the roughness has to be done differently.

The engraved surface morphology can be perceived as a superposition of many individual craters. We have already seen that once the roughness stabilization is achieved, the roughness value is determined by the overlap of the craters. However, the peak-to-valley height of the surface corresponds to the depth of a single crater, which can be fine tuned using different pulse energies and change in wavelengths. Profiles of the ablated craters produced with a single pulse using different pulse energies and wavelengths are depicted in Fig. 8(A). Since the ablated cavities were symmetrical, only profiles were investigated. Based on the visual representation, the crater sidewalls exhibit a small level of roughness (R_a was measured to be < 10 nm), akin to the presence of background noise.

When using lower pulse energies or shorter wavelengths, the shape of the crater reduces not only in a longitudinal direction but also in a depth. To maintain the necessary overlap of the craters, the reduction of the crater's width has to be compensated by decreasing the scanning speed. If all conditions are satisfied, the induced (defined by the overlap) surface shape is maintained and only the peak-to-valley distance is varied. The measured surface roughness evolution of such a case is depicted in Fig. 8(B). As seen from the figure, when lower pulse energies are used, the resulting surface roughness can be further reduced. This allows for further tuning of the surface roughness stabilization level. However, the available range of fluence values between the non-ablation regime and the maximum achievable depth, restricted by optical penetration depth, is narrow. Moreover, when using IR laser radiation, ablation with lower fluence values near the ablation threshold results in the inconsistency of crater geometry with low repeatability of crater shape. The aforementioned factors establish the boundaries for the variety of crater depths attainable by manipulating the pulse energy using IR ($\lambda = 1030$ nm) laser radiation. It has been demonstrated that the optical penetration depth, as well as ablation threshold of the dielectrics, can be reduced by using shorter wavelength radiation, allowing for the generation of smaller scale craters in a controlled manner [37]. By utilizing these findings we were able to produce even smaller craters (with depths down to 20 nm) using UV ($\lambda = 343$ nm) radiation, thus extending the boundaries for the tunability of the surface roughness stabilization level. The determined relation between surface roughness and the depth of a single crater is depicted in Fig. 8(C). As can be seen from the figure, there is a 1-to-1 correlation between surface roughness and the depth of a single crater: a nearly linear increase is observed at intermediate crater depth values with a tendency to saturate at deeper values. However, the minimum roughness ($S_a \sim 130$ nm) is reached when the depth of the crater matches $H \sim 130$ nm, and any further reduction in the crater's depth no longer results in decreased roughness, setting the lower boundary for the attainable minimum roughness using the presented methods.

The reason for this limit is the appearance of nanostructure as can be seen in electronic microscope pictures in Fig. 9. The islands of nanoripples appear after the initial few layers of engraving, reducing the homogeneity of the surface. However, with continuous processing, these islands tend to grow towards nonregular nanostructure patern which saturates the total roughness. In addition, the energy dispersive X-ray spectroscopy (EDS) comparison of deep-ablated and non-treated surfaces shows the composition changes in the material (Fig. 10).
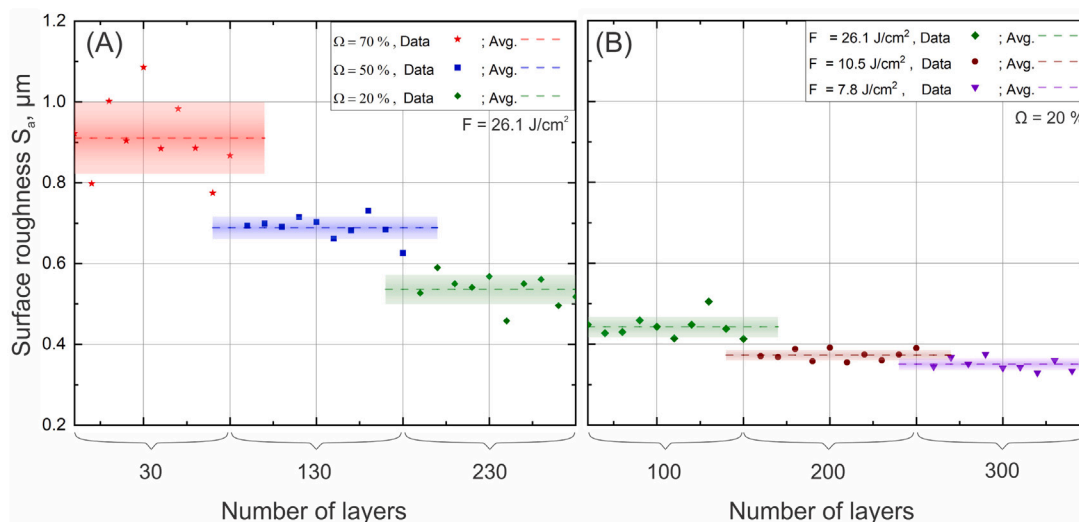
Fig. 11. Surface roughness dependence on the number of scans when different scanning algorithms are used. Graph (A) shows engraving with different overlaps of the craters, while graph (B) shows when different pulse energies are used. In both cases, scanning with different algorithm parameters was performed on previously engraved surfaces in continuous succession (see text for clarification). Dots represent raw data, while dashed lines — average values. The extent of the colored area surrounding the average values stands for a range equivalent to one standard deviation. Other processing parameters: $\alpha = 73°$, $\lambda = 1030$ nm. The uncertainty of layer positioning of a maximum magnitude $\Delta \geq dx$ was maintained.
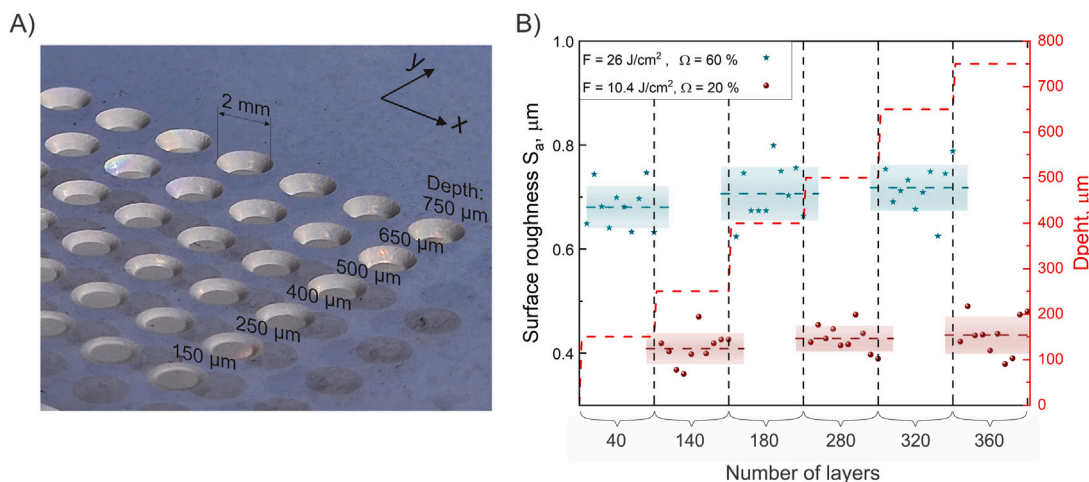
Fig. 12. (A) A photo of the sample after deep-engraving. In the y direction, cavities of different depths can be seen, whereas in the x direction, cavities ablated using identical parameter sets are shown. In part (B) of the figure, surface roughness and depth of the cavity dependencies on the number of scans are presented. Dots represent raw data, while dashed lines — averaged values. The extent of the colored area surrounding the average values stands for a range equivalent to one standard deviation. Other processing parameters: $\alpha = 73°$, $\lambda = 1030$ nm. The uncertainty of layer positioning of a maximum magnitude $\Delta \geq dx$ was maintained. (For interpretation of the references to color in this figure legend, the reader is referred to the web version of this article.)

Mainly the decrease in oxygen content on the glass surfaces is observed, indicating the increased presence of oxygen-deficient centers, which are known to appear in self-organized nanostructures in fused silica [38].

Finally, the established methods to control the surface roughness were put to the test while deep engraving fused silica glass. In this experiment, to determine the repeatability of the process, ten regions underwent deep engraving using identical scanning parameters and the roughness was subsequently measured as shown in Fig. 11. To illustrate the ability to control surface roughness the previously ablated surface was additionally processed with a different set of scanning parameters in a continuous fashion.

In Fig. 11(A), a case is shown where the surface is repeatedly engraved using different crater's overlaps. A typical number of layers necessary for the attainment of the surface roughness stabilization is up to 30, depending on the laser and scanning parameters used. Nevertheless, to ensure the complete stabilization each scanning algorithm was repeated for 100 layers. The only exception was for 70%

overlap case because due to efficient ablation a 1 mm thick sample is thoroughly ablated within 100 layers, therefore only 30 layers were used. Before applying every next scanning algorithm, the lens was repositioned by moving the z-axis to ensure that the surface stays in the focal plane of the lens. The experiment was conducted in such a way that initially the scanning parameter set that produces the highest roughness was used first (in this case 30 layers of $\Omega = 70\%$). The results were measured, a new set of scanning parameters was selected and an additional 100 layers were ablated on top of the previously processed surface (100 more layers with $\Omega = 50\%$). The procedure was repeated for another 100 layers at $\Omega = 20\%$. From the results, it is clear that by using different scanning algorithms (i.e. different overlap values) roughness stabilization at different values can be achieved. Moreover, using an optimized scanning algorithm, the reduction of roughness can be achieved producing polishing effect. This observation implies that determined scanning methods achieve success in their operation, regardless of whether the starting surface is flat or rough.

A similar experiment was done where different scanning algorithms included the change of crater depth by reducing the pulse energy (Fig. 11(B)). As before, the initial parameter set was selected to yield the maximum surface roughness and the first 100 layers were ablated. Proceeding that, the pulse energy was reduced, and additional scans were conducted on the already processed surface. The engraving involved 3 steps comprising different values of pulse energies, resulting in the stabilization of the roughness at different levels. In this case, we can see that the difference between the stabilization levels is significantly smaller. Showcasing that by varying the pulse energy, the fine-tuning of the roughness stabilization level can be achieved, while changing the overlap of the craters results in a more coarse adjustment of the roughness stabilization value. These observations agree well with the previous discussion. The findings suggest that by utilizing different scanning algorithms, namely inducing different roughness via control of the overlap of the craters and tuning crater depth by adjusting pulse energy, the fine ($\delta S_a = 20$ nm) control of the roughness stabilization level within a wide range of roughness values ($300 \div 900$ nm) is achievable.

Such roughness stabilization is possible at various depths in deep-engraving applications. To demonstrate that, the samples were engraved up to 750 μm in depth while controlling the surface roughness via a change of scanning algorithm. The results are shown in Fig. 12. Each experiment was repeated 10 times to investigate its reproducibility. While engraving the material, the surface roughness was varied between two stable roughness levels of our choice. The combination of $E_p = 181$ μJ (F = 26 J/cm^2) and $\Omega = 60\%$ resulted in the roughness of $S_a \sim 700$ nm, whereas the combination of $E_p = 72.5$ μJ (F = 10.4 J/cm^2) and $\Omega = 20\%$ produced roughness of $S_a \sim 420$ nm. Before changing the scanning algorithm, the bottom part of the micromachined area was repositioned back to the focal plane of the lens to compensate for the divergence of the beam. Each successive scanning step was performed on a surface processed by the previous scanning algorithm. A photo of a deeply engraved sample is shown in Fig. 12(A), while Fig. 12(B) shows how the surface roughness was varied during engraving. It can be seen that throughout the engraving process, the roughness was changed 6 times. In addition, the roughness was not only reduced but also enlarged in a controlled manner via a change in the scanning algorithm. By the end of the deep-engraving experiment, the roughness of $S_a = 420$ nm at the depth of 750 μm was achieved. Demonstrated results show that full control (reduction as well as enlargement) of surface roughness while engraving can be achieved by applying the strategies presented in this paper.

During the study, the methods for the control of the surface roughness for laser engraving were presented. The methods include the combination of rotation of the layers, the introduction of the uncertainty of layer positioning, the varying overlap of the craters as well as pulse energy and wavelength of the laser radiation. While the presented methods allow for the control of surface roughness, a few things have to be noted. The primary condition for these methods to work is that the sidewalls and the overall geometry of a single crater have to be of high quality and repeatability. This is usually the case when ablating dielectrics like glass and crystals with femtosecond laser radiation. However, when ablating metals, the quality tends to be worse [39], making it challenging for the application of the presented methods. In addition, when arbitrary shape regions have to be ablated the scanning pattern has to be rotated and cropped to the designated shape: it could be easily realized using CAD shape hatching functionality available in many commercial laser scanning software. Lastly, we have demonstrated that the lowest attainable roughness is constrained by the development of the nanoripples, which subsequently give rise to a consistent nanostructure across the entire surface, whose roughness serves as a determining factor in defining the overall roughness of the surface in the investigated case of fused silica. While the solution for the prevention of nanoripple formation is not yet available, the challenge will serve as a goal for future research endeavors.

4. Conclusions

In conclusion, methods for the control of the surface roughness while deep engraving were developed. The stabilization of the surface roughness can be achieved by selecting a scanning algorithm that includes the rotation of every subsequent layer at an angle of category 1 (example being a primary number), with the addition of the introduction of layer positioning uncertainty with a magnitude of $\Delta \geq dx$. Under such conditions, the formation of periodic patterning artefacts is prevented and the stabilization of the roughness is achieved within the first 30 layers. The level at which the roughness will stabilize is determined by the initial overlap of the craters and their depths. The former can be scaled by tailoring pulse energy or adjusting the wavelength to smaller values, reducing the light penetration depth. The broad range of different roughness values ($\Delta S_a \sim 550$ nm) was attained with a resolution of $\delta S_a = 20$ nm under deep-engraving conditions. The appearance of self-organized nanostructures after multipulse ablation remains the limiting factor for the minimum attainable roughness ($S_a = 130$ nm).

CRediT authorship contribution statement

Evaldas Kažukauskas: Writing – review & editing, Writing – original draft, Investigation, Formal analysis. **Simas Butkus:** Writing – original draft, Supervision, Methodology, Data curation, Conceptualization. **Vytautas Jukna:** Writing – review & editing, Writing – original draft, Visualization, Software, Formal analysis. **Domas Paipulas:** Writing – review & editing, Writing – original draft, Visualization, Project administration, Funding acquisition, Formal analysis, Conceptualization.

Declaration of competing interest

The authors declare that they have no known competing financial interests or personal relationships that could have appeared to influence the work reported in this paper.

Data availability

No data was used for the research described in the article.

References

[1] I. Okokpujie, C. Bolu, O. Ohunakin, E. Akinlabi, D. Adelekan, A review of recent application of machining techniques, based on the phenomena of CNC machining operations, Procedia Manuf. 35 (2019) 1054–1060, http://dx.doi.org/10.1016/j.promfg.2019.06.056.

[2] C. Hsu, F. Chang, Y. Huang, Surface machining of stainless steel cardiovascular stents by fluid abrasive machining and electropolishing, Key Eng. Mater. 897 (2021) 3–13, http://dx.doi.org/10.4028/www.scientific.net/KEM.897.3.

[3] C. Baley, F. Busnel, Y. Grohens, O. Sire, Influence of chemical treatments on surface properties and adhesion of flax fibre–polyester resin, Composites A 37 (10) (2006) 1626–1637, http://dx.doi.org/10.1016/j.compositesa.2005.10.014.

[4] M. Colburn, T. Bailey, B. Choi, J. Ekerdt, S.V. Sreenivasan, C. Willson, Development and advantages of step-and-flash lithography, Solid State Technol. 44 (7) (2001).

[5] N. Ahmed, S. Darwish, A.M. Alahmari, Laser ablation and laser-hybrid ablation processes: A review, Mater. Manuf. Process. 31 (9) (2016) 1121–1142, http://dx.doi.org/10.1080/10426914.2015.1048359.

[6] A. Toloei, V. Stoilov, D. Northwood, The relationship between surface roughness and corrosion, in: Proceedings of the Asme International Mechanical Engineering Congress and Exposition, 2013, Vol 2B, 2013, V02BT02A054, http://dx.doi.org/10.1115/IMECE2013-65498.

[7] Q. Cao, S. Zheng, C.-P. Wong, S. Liu, Q. Peng, Massively engineering the wettability of titanium by tuning nanostructures and roughness via laser ablation, J. Phys. Chem. C 123 (50) (2019) 30382–30388, http://dx.doi.org/10.1021/acs.jpcc.9b08580.

[8] J. Altmeppen, H. Sommerfeld, C. Koch, S. Staudacher, Experimental and numerical investigation into the effect of surface roughness on particle rebound, Front. Mech. Eng. 8 (2022) http://dx.doi.org/10.3389/fmech.2022.918708.

[9] Y. Huang, S. Liu, W. Yang, C. Yu, Surface roughness analysis and improvement of PMMA-based microfluidic chip chambers by CO_2 laser cutting, Appl. Surf. Sci. 256 (2010) 1675–1678, http://dx.doi.org/10.1016/j.apsusc.2009.09.092.

[10] C. Kleinstreuer, J. Koo, Computational analysis of wall roughness effects for liquid flow in micro-conduits, J. Fluids Eng. 126 (1) (2004) 1–9, http://dx.doi.org/10.1115/1.1637633.

[11] D. Bergström, J. Powell, A.F. Kaplan, The absorption of laser light by rough metal surfaces, J. Appl. Phys. 103 (10) (2008) 103515, http://dx.doi.org/10.1063/1.2930808.

[12] M. Auinger, P. Ebbinghaus, A. Blümich, A. Erbe, Effect of surface roughness on optical heating of metals, J. Eur. Opt. Soc. 9 (2014) http://dx.doi.org/10.2971/jeos.2014.14004.

[13] E. Kažukauskas, S. Butkus, P. Tokarski, V. Jukna, M. Barkauskas, V. Sirutkaitis, Micromachining of transparent biocompatible polymers applied in medicine using bursts of femtosecond laser pulses, Micromachines 11 (12) (2020) http://dx.doi.org/10.3390/mi11121093.

[14] A.H.A. Lutey, L. Gemini, L. Romoli, G. Lazzini, F. Fuso, M. Faucon, R. Kling, Towards laser-textured antibacterial surfaces, Sci. Rep. 8 (1) (2018) 10112, http://dx.doi.org/10.1038/s41598-018-28454-2.

[15] A. Mohammad, M.K. Mohammed, A. Al-Ahmari, Effect of laser ablation parameters on surface improvement of electron beam melted parts, Int. J. Adv. Manuf. Technol. 87 (2016) http://dx.doi.org/10.1007/s00170-016-8533-4.

[16] M.N.F.B. Haron, F.R.B.M. Romlay, Parametric study of laser engraving process of AISI 304 Stainless Steel by utilizing fiber laser system, IOP Conf. Ser.: Mater. Sci. Eng. 469 (1) (2019) 012124, http://dx.doi.org/10.1088/1757-899X/469/1/012124.

[17] A. Žemaitis, M. Gaidys, P. Gečys, G. Račiukaitis, M. Gedvilas, Rapid high-quality 3D micro-machining by optimised efficient ultrashort laser ablation, Opt. Lasers Eng. 114 (2019) 83–89, http://dx.doi.org/10.1016/j.optlaseng.2018.11.001.

[18] M. Domke, G. Piredda, J. Zehetner, S. Stroj, Minimizing the surface roughness for silicon ablation with ultrashort laser pulses, J. Laser Micro Nanoeng. 11 (1) (2016) 100.

[19] D. Kam, L. Shah, J. Mazumder, Femtosecond laser machining of multi-depth microchannel networks onto silicon, J. Micromech. Microeng. 21 (4) (2011) 045027.

[20] S. Campanelli, G. Casalino, N. Contuzzi, A. Ludovico, Taguchi optimization of the surface finish obtained by laser ablation on selective laser molten steel parts, Procedia CIRP 12 (2013) 462–467, http://dx.doi.org/10.1016/j.procir.2013.09.079.

[21] S. Kasman, Impact of parameters on the process response: A Taguchi orthogonal analysis for laser engraving, Measurement 46 (8) (2013) 2577–2584, http://dx.doi.org/10.1016/j.measurement.2013.04.022.

[22] X. Li, H. Wang, B. Wang, Y. Guan, Machine learning methods for prediction analyses of 4H–SiC microfabrication via femtosecond laser processing, J. Mater. Res. Technol. 18 (2022) 2152–2165, http://dx.doi.org/10.1016/j.jmrt.2022.03.124.

[23] A. Caggiano, R. Teti, V. Alfieri, F. Caiazzo, Automated laser polishing for surface finish enhancement of additive manufactured components for the automotive industry, Prod. Eng. 15 (2020) http://dx.doi.org/10.1007/s11740-020-01007-1.

[24] V. Narayanan, R. Singh, D. Marla, A computational model to predict surface roughness in laser surface processing of mild steel using nanosecond pulses, J. Manuf. Process. 68 (2021) 1880–1889, http://dx.doi.org/10.1016/j.jmapro.2021.07.016.

[25] G. Schnell, U. Duenow, H. Seitz, Effect of laser pulse overlap and scanning line overlap on femtosecond laser-structured Ti_6Al_4V surfaces, Materials 13 (4) (2020) http://dx.doi.org/10.3390/ma13040969.

[26] E. Kažukauskas, S. Butkus, V. Jukna, D. Paipulas, V. Sirutkaitis, Scanning algorithm optimization for achieving low-roughness surfaces using ultrashort laser pulses: A comparative study, Materials 16 (7) (2023) 2788, http://dx.doi.org/10.3390/ma16072788.

[27] B. Jaeggi, B. Neuenschwander, U. Hunziker, J. Zuercher, T. Meier, M. Zimmermann, K.H. Selbmann, G. Hennig, Ultra-high-precision surface structuring by synchronizing a galvo scanner with an ultra-short-pulsed laser system in MOPA arrangement, in: Proc. SPIE 8243, Laser Applications in Microelectronic and Optoelectronic Manufacturing (LAMOM) XVII, Vol. 8243, 2012, 82430K, http://dx.doi.org/10.1117/12.909844.

[28] S. Campanelli, A. Ludovico, C. Bonserio, P. Cavalluzzi, M. Cinquepalmi, Experimental analysis of the laser milling process parameters, J. Mater. Process. Technol. 191 (1) (2007) 220–223, http://dx.doi.org/10.1016/j.jmatprotec.2007.03.005.

[29] F.A. Sfregola, R. De Palo, C. Gaudiuso, F.P. Mezzapesa, P. Patimisco, A. Ancona, A. Volpe, Influence of working parameters on multi-shot femtosecond laser surface ablation of lithium niobate, Opt. Laser Technol. 177 (2024) 111067, http://dx.doi.org/10.1016/j.optlastec.2024.111067.

[30] D. Pallarés-Aldeiturriaga, P. Claudel, J. Granier, J. Travers, L. Guillermin, M.-O. Flaissier, P.B. d'Augeres, X. Sedao, Femtosecond laser engraving of deep patterns in steel and sapphire, Micromachines 12 (7) (2021) http://dx.doi.org/10.3390/mi12070804.

[31] J.M. Liu, Simple technique for measurements of pulsed Gaussian-beam spot sizes, Opt. Lett. 7 (5) (1982) 196–198, http://dx.doi.org/10.1364/OL.7.000196.

[32] G. Schnell, U. Duenow, H. Seitz, Effect of laser pulse overlap and scanning line overlap on femtosecond laser-structured Ti_6Al_4V surfaces, Materials 13 (2020) 969, http://dx.doi.org/10.3390/ma13040969.

[33] C.L. Giusca, J.D. Claverley, W. Sun, R.K. Leach, F. Helmli, M.P. Chavigner, Practical estimation of measurement noise and flatness deviation on focus variation microscopes, CIRP Ann 63 (1) (2014) 545–548, http://dx.doi.org/10.1016/j.cirp.2014.03.086.

[34] J. Bonse, S. Höhm, S.V. Kirner, A. Rosenfeld, J. Krüger, Laser-induced periodic surface structures— A scientific evergreen, IEEE J. Sel. Top. Quantum Electron. 23 (3) (2017) http://dx.doi.org/10.1109/JSTQE.2016.2614183.

[35] F. Liang, R. Vallée, S.L. Chin, Mechanism of nanograting formation on the surface of fused silica, Opt. Express 20 (4) (2012) 4389–4396, http://dx.doi.org/10.1364/OE.20.004389.

[36] F. Liang, R. Vallée, Physical origin of nanograting formation on fused silica with femtosecond pulses, Appl. Phys. Lett. 105 (13) (2014) 131904, http://dx.doi.org/10.1063/1.4896749.

[37] M. Fox, Optical Properties of Solids, Oxford University Press, 2010.

[38] Y. Shimotsuma, K. Hirao, J. Qiu, P.G. Kazansky, Nano-modification inside transparent materials by femtosecond laser single beam, Modern Phys. Lett. B 19 (05) (2005) 225–238, http://dx.doi.org/10.1142/S0217984905008281.

[39] M.E. Shaheen, J.E. Gagnon, B.J. Fryer, Laser ablation of iron: A comparison between femtosecond and picosecond laser pulses, J. Appl. Phys. 114 (8) (2013) 083110, http://dx.doi.org/10.1063/1.4819804.